JOURNAL OF PROPULSION AND POWER
Vol. 16, No. 1, January–February 2000

Aerodynamic Analysis of an Installed Thrust Reverser

Daniel J. Strash* and J. Michael Summa†
Analytical Methods, Inc., Redmond, Washington 98052
and
Joel H. Frank‡ and Robert Standish‡
Hurel-Dubois, 92363 Meudon-la-Forêt CEDEX, France

One of the most challenging problems for modern computational fluid dynamics methods is the accurate calculation of installed thrust-reverser performance. In this paper, a three-dimensional Cartesian grid Euler method is used to compute the flow about a contemporary business jet with thrust reversers deployed in ground effect. While the entire aircraft is included in this simulation, the multigrid procedure facilitates grid refinement near the thrust-reverser components. Further, the Cartesian grid structure can be assembled in a few days and preliminary design solutions computed in 1–2 h of Cray J90 time. More detailed solutions may be obtained via program restarts. Regardless, subsequent solutions at other design points or with minor design modifications are achieved within 1-day elapsed time. For the case analyzed, computed particle traces are qualitatively similar to exhaust plume trajectories observed in tests on similar installations. Furthermore, the computed pressure distribution on the windward side of the thrust-reverser door compares favorably with available test data, and the computed net braking force is within 2% of the measured data. Based on these data comparisons and the practical user/computational requirements of the method, numerical simulations of installed thrust reverser applications are feasible for preliminary designs.

Nomenclature

C_D	= drag coefficient
C_L	= aircraft lift coefficient
C_p	= pressure coefficient, $(p - p_\infty)/\frac{1}{2}\rho_\infty q_\infty^2$
C_V	= reverser efficiency
d	= exhaust diameter
$\boldsymbol{E}$	= flux vector
e	= total energy per unit mass
$\hat{\boldsymbol{e}}_x, \hat{\boldsymbol{e}}_y, \hat{\boldsymbol{e}}_z$	= unit vector in the Cartesian system
$\boldsymbol{F}$	= $(\rho, \rho u, \rho v, \rho w, \rho e)$ vector of Euler variables formula
h	= total enthalpy
M	= Mach number
$\hat{n}$	= outward surface normal
P	= pressure
$\boldsymbol{q}$	= stream velocity vector
R	= specific gas constant
S	= surface designation
s	= entropy
T	= temperature
t	= time
u, v, w	= components of $\boldsymbol{q}$ in global coordinates x, y, z
V	= volume of surface S
x, y, z	= global coordinates: x along the body axis, y spanwise, and z up
α	= angle of attack
γ	= ratio of specific heats
$\partial/\partial t$	= partial derivative with respect to time
ρ	= density

Subscripts

t	= total conditions
∞	= freestream value

Superscript

T	= transpose

Introduction

FOR decades, conventional brake systems on commercial transport aircraft have been supplemented by thrust-reverser technology. These engine components improve aircraft safety for wet or icy runway operating conditions and can enhance aircraft maneuverability during ground roll. Thrust-reverser design involves the conflicting objectives of maximizing reverser efficiency while minimizing the cruise drag penalty, noise, the adverse effects on engine performance and aircraft stability and control, and the weight of the reverser components.[1]

Typically, designers make full use of wind-tunnel and flight-test methods throughout the design process.[1,2] Numerical methods have been applied in a more limited fashion ranging from two-dimensional Navier–Stokes[2,3] to three-dimensional body-fitted Euler and Navier–Stokes methods.[4] However, numerical simulations of thrust reverser operations are extremely complicated in that the geometries are complex and the flow is strongly three dimensional and highly turbulent. For example, the interaction between the vectored exhaust plume and the freestream flow is dominated by turbulent mixing, and the leeward side of the reverser door may be immersed in separated flow. Generally, the fine geometric details such as kicker plates that are required in reverser simulations preclude the use of body-fitted grid methods in a design environment. Consequently, simpler numerical methods are investigated to determine their accuracy for these applications. For example, a three-dimensional Euler simulation of an isolated nacelle with a four-door thrust reverser is reported in Ref. 5.

The work reported here uses a three-dimensional Cartesian Euler method[6] to investigate the aerodynamic behavior of an installed, deployed thrust reverser with kicker plates. Viscous effects are undoubtedly important in determining some local surface pressures and in computing heat transfer, jet plume effects and component

Presented as Paper 97-3153 at the AIAA/ASME/SAE/ASEE 33rd Joint Propulsion Conference, Seattle, WA, 6–9 July 1997; received 10 February 1998; revision received 21 December 1998; accepted for publication 4 January 1999.

*Senior Research Scientist, 2133 152nd Avenue, NE.
†Vice President Aerospace Technology, 2133 152nd Avenue, NE.
‡Aerodynamics Engineer, 13-21, avenue du Maréchal-Juin.

load estimations for installed thrust reversers can be predicted with a Euler method. Furthermore, because of the simplicity of the method employed here, preliminary design simulations of installed thrust reversers are practical on existing computers.

Method

The computer code employed in this work uses a multigrid calculation procedure with an equally spaced Cartesian mesh structure to discretize the governing Euler equations for inviscid compressible flow. Swept, unswept, or rotated grids compose local computational domains that may be overlapped with boundary surfaces and/or other multigrid levels.

The versatility of the method in handling complicated configurations is due largely to its use of Cartesian and sheared Cartesian grids. Because the program does not require grids aligned to the body surface, grid generation is much simpler than with other computational fluid dynamics (CFD) methods. Uniformly meshed grids formally lead to second-order-accurate approximations of the governing Euler equations.

The program consists of two distinct stages. The first is a preprocessor, which generates the interpolation functions, for both the transfer of information between grids and for the surface-to-grid relationship. The preprocessor interprets the configuration as the Boolean sum of all components and automatically computes any intersections. Therefore, the process of specifying the geometry of complex configurations is straightforward. The user represents each component by a surface panelization without regard to intersection details.

To achieve greater resolution without the necessity of generating unmanageably large numbers of flowfield grid points, this method makes extensive use of local refinement within the framework of the multigrid approach. This leads to more efficient use of computer resources because the finest grids are placed only in regions where the flow properties are varying rapidly.

The grids are grouped in levels, with each level characterized by a particular mesh size. The coarsest level-one grid consists of a single Cartesian grid block. Its outer boundaries should be far enough from the configuration to be considered in undisturbed flow, unless some physical border, e.g., wind-tunnel walls, bound the flowfield. Subsequent finer-grid levels may consist of multiple-grid blocks, all contained within the previous course-grid level. The ratio between cell edge lengths from a fine- to coarse-grid level is typically 2:1.

The second stage is the multigrid solver, which uses the preprocessor information to generate a flow solution. Within the multigrid algorithm, the discretized Euler equations iteratively approach steady state via a four-stage Runge–Kutta scheme. Through its use of solution interpolation, the multigrid approach ensures the integrity of the flow solution at grid boundaries and regions of grid overlap. Thus, this method has the advantage of convergence acceleration present in classical multigrid techniques without the expense of extensive grid refinement throughout the flow domain.

Clearly, the solver can calculate various flight conditions without repeating the preprocessor stage. Moreover, the program allows solution restarts either proceeding to subsequent multigrid levels with finer grid resolution or continuing with further iterations at the current level. Both the preprocessor and solver codes generate output and plot files that allow detailed examination of the results.

The Euler equations that are solved by the present method govern inviscid, compressible fluid motion and are written in integral form for the general control volume V, whose surface S has an outward unit normal $\hat{\boldsymbol{n}}$ as

$$\frac{\partial}{\partial t}\iiint_{\text{vol}} \boldsymbol{F}\,\mathrm{d}V + \iint_{s} \boldsymbol{E}\cdot\hat{n}\,\mathrm{d}S = 0 \tag{1}$$

where $\boldsymbol{F}$ is the vector of dependent variables

$$\boldsymbol{F}^T = \{\rho, \rho u, \rho v, \rho w, \rho e\} \tag{2}$$

and $\boldsymbol{E}$ is the flux vector

$$\boldsymbol{E} = \begin{Bmatrix} \rho\boldsymbol{q} \\ \rho u\boldsymbol{q} + p\hat{\boldsymbol{e}}_x \\ \rho v\boldsymbol{q} + p\hat{\boldsymbol{e}}_y \\ \rho w\boldsymbol{q} + p\hat{\boldsymbol{e}}_z \\ \rho h\boldsymbol{q} \end{Bmatrix} \tag{3}$$

with unit vectors $\hat{\boldsymbol{e}}_x$, $\hat{\boldsymbol{e}}_y$, and $\hat{\boldsymbol{e}}_z$ along the coordinate axes, and $\boldsymbol{q}$ the velocity vector with Cartesian components (u, v, w). This expression represents a system of equations corresponding to conservation of mass, momentum and energy. Here, the Cartesian coordinate system is denoted by (x, y, z); q is the magnitude of the velocity vector $\boldsymbol{q}$; p and ρ are the pressure and density; and h is the total enthalpy. The equation for total enthalpy is

$$h = e + (p/\rho) = [\gamma/(\gamma - 1)](p/\rho) + \tfrac{1}{2}q^2 \tag{4}$$

where γ is the ratio of specific heats ($\gamma = 1.4$ for air), and e is the total energy per unit mass. Finally, for closure the ideal gas equation of state is

$$p = \rho RT \tag{5}$$

where R is the specific gas constant ($R = 1716$ ft^2/s^2°R for air).

Because these equations are written in conservation form, they also preserve the correct jump conditions (Rankine–Hugoniot) across a discontinuity. Thus, this technique is a shock-capturing approach that is predominant in computational aerodynamics rather than the shock-fitting method that requires tracking a discontinuity within the flow and explicitly enforcing jump conditions to obtain the downstream properties.

Test Apparatus

The experimental database for this configuration consists of a 1:12 scale wind-tunnel test,[7] and two separate 1:12 scale[8] and 1:5 scale[9] static thrust tests. This study utilized data primarily from the wind-tunnel test and from the 1:5 scale static thrust test.

The wind-tunnel test employed a 1:12 scale aircraft model owned by the Netherland Agency for Aerospace Programmes, and testing[7] was carried out in the Duits-Nederlandse Windtunnel (DNW) Low Speed Wind Tunnel (LST) located at the North East Polder site in Holland. The wind tunnel is a closed-return type and runs at atmospheric conditions. The test section measures 9.8 ft across, 7.4 ft in height, and has a total length of 28.7 ft. The maximum attainable wind speed is 256 ft/s.

The 1:12 scale aircraft model included axisymmetric nacelles composed of both inlet and exhaust assemblies and an internal flow package to provide acceptable flow profiles to the thrust reversers. Both inlets were flowing. No provision was made to tune the two inlets to each other, although the two nacelles were calibrated in isolation on a static thrust stand. The model also incorporated adjustable wing trailing-edge flaps, spoilers, and tail horizontal stabilizers. For hot gas reingestion testing, the model was mounted in an upright position in close proximity to a nonmoving ground plane of fixed height. A typical touchdown clearance was set using the three adjustable supports, which secured the model to the ground board.

The one-fifth-scale model static thrust performance test at FluiDyne[9] included a dual hot-flow air supply with a three-component force measurement system capable of recording axial force, vertical force, and pitching moment. The instrumentation also included pressure taps on the inner surface of the upper thrust-reverser door. Further, the thrust-reverser plenum was rigged with a single static pressure tapping for measuring upstream delivery pressure to the exhaust flow package. Finally, the exhaust instrumentation consisted of four fixed rake assemblies, each rake housing two total pressure probes and one total temperature probe. This instrumentation allowed individual jet velocities and exhaust nozzle pressure ratios to be calculated.

Results

Case Description

Calculations presented here are for an aircraft with deployed thrust reversers in ground effect at a freestream Mach number of 0.15. The inflow speed and the fan and core pressure and temperature ratios for this case are prescribed according to the wind-tunnel test data and are presented below in Table 1. For subsonic boundary conditions, the Euler equations require four specified variables at the engine exhaust face and one at the engine inlet boundary. The boundary conditions allowed by the current method require that the radial components of velocity on the inflow and outflow faces are zero. Further, for both calculations, the circumferential components of velocity on the inflow and outflow faces were neglected.

The installed thrust reverser is presented in Fig. 1 along with the Cartesian grid layout for the level 7 calculation. The thrust-reverser doors with advanced kicker-plate geometry are deployed at 60 deg to the engine exhaust flow (see Fig. 1b). In the numerical model, the kicker plate thickness was artificially increased as a workaround for a code deficiency that has subsequently been removed. Nevertheless, this geometric change would insignificantly affect the computed flow solution. The test results primarily consisted of elements of the thrust-reverser braking force, some surface-pressure data, and a qualitative description of the plume trajectory. Thus, the level 7 grid, which represents the finest grid resolution, is concentrated in the vicinity of the deployed thrust-reverser door and in the region of the exhaust plume (see Fig. 1c). The final numerical model consisted of nearly 2×10^6 grid points and required 435 MB of memory. The computational time at this grid resolution for the Mach 0.15 flight condition was about 18 h on a Cray J90.

Table 1 Engine flow conditions

		Fan exit		Primary exit	
Description	Inflow, ft/s	P_t / P_∞	T_t / T_∞	P_t / P_∞	T_t / T_∞
Ground effect	337.6	1.52	1.19	1.40	2.62

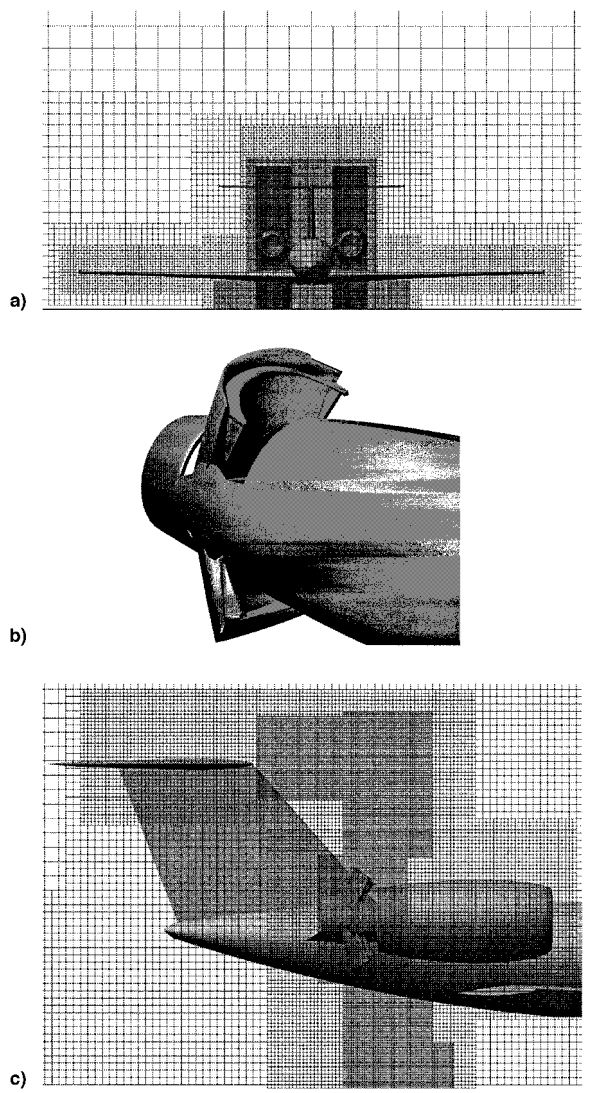

Fig. 1 Installed thrust reverser in ground effect, a) front view with grid, b) close-up view, and c) side view with grid.

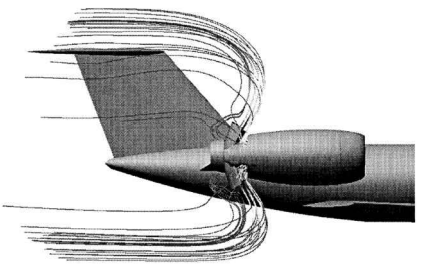

Fig. 2 Computed exhaust plume trajectory (Mach 0.15, ground effect).

Plume Trajectory

The plume trajectory in the presence of the complete aircraft in ground effect is displayed in Fig. 2. The computed trajectory for the upper plume is qualitatively similar to that observed under test conditions.[7] However, the lower plume consisted of a recirculation zone between the wing and ground plane, which is not in the computed result. The effects of deployed wing spoilers and nonmoving ground plane on the wind-tunnel test trajectories are not included in the computation and may account for these differences.

Further insight into the local door flow characteristics may be obtained by examining the computed flow vectors. Constant-length flow vectors are presented for an upper, mid door waterline and a door centerline section in Fig. 3. The dominant feature is the door lateral-edge vortices shown in Fig. 3a. The side view, Fig. 3b, indicates that these vortices track up the axis of the jet plume. Clearly, the flowfield is highly three dimensional and precludes the use of two-dimensional methods for analysis and design of such thrust reverser doors.

Door Pressures

The computed variation in upper, starboard door, surface-pressure coefficient is compared with experimental data[9] at five different stations in Figs. 4–8. The experimental data are from a scale engine test at static conditions and with a 16-lobe daisy mixer and the current simulation is at 100 kn, the jet thrust conditions are equivalent for the test and calculation. The specific pressure tap locations are presented in the inset of each figure. Here, the view is looking downstream with the aircraft to the right. Also, the geometric overlaps that are allowed in this method are clearly illustrated in these figures. As further verification of the solution convergence characteristics, the computed door surface-pressure variation is displayed at progressively finer grid levels in Fig. 4. Grid levels 5 and 6 and grid levels 6 and 7 are shown in Figs. 4a and 4b, respectively. Each subsequent grid refinement results in an improved estimation of the door surface-pressure distribution as indicated by the correlation to the test data.

As illustrated in Figs. 4–8, the computed pressure variations at the experimental data locations compare favorably with the measurements. Quantitatively, the pressures compare more accurately for the lower three-quarters of the door, which is directly impacted by the jet exhaust. Here, the differences between the computed and measured pressures fall within 10%. On the other hand, these pressure differences increase to roughly 30% for the single measured data point nearest the kicker plate. This degradation in the comparison is most likely due to the inability of the inviscid Euler equations to model the vortex observed at the base of the kicker plate[9] As

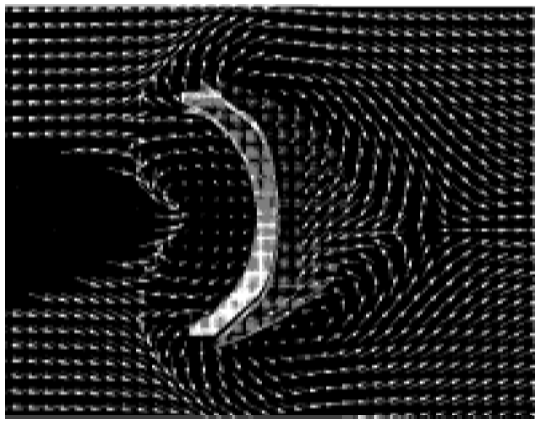

a)

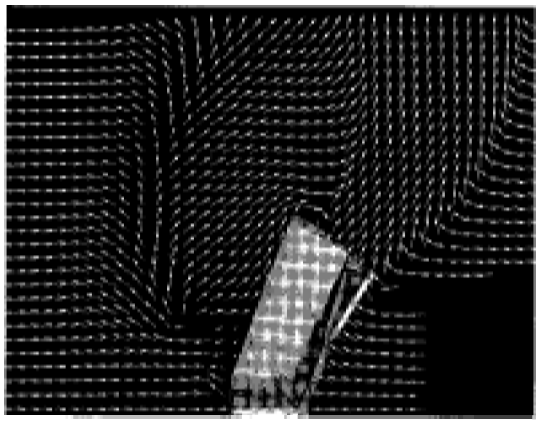

b)

Fig. 3 Flow details in vicinity of upper thrust-reverser door (Mach 0.15, ground effect) a) top view with flow from left to right and b) side view with flow from right to left.

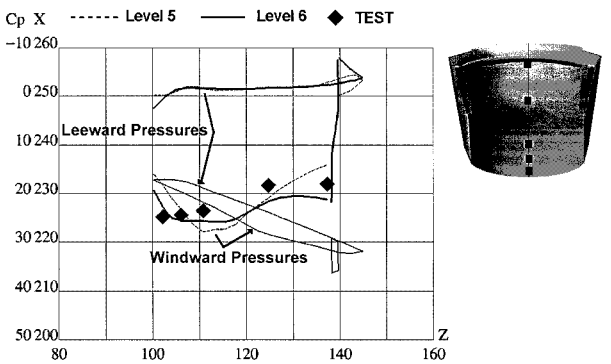

a)

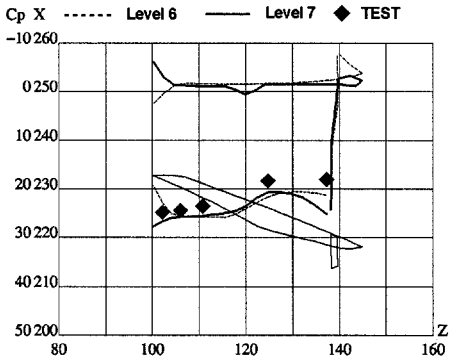

b)

Fig. 4 Comparison of computed and experimental pressure distribution on reverser door for station 1 (Mach 0.15, ground effect) a) numerical grid levels 5 and 6 and b) numerical grid levels 6 and 7.

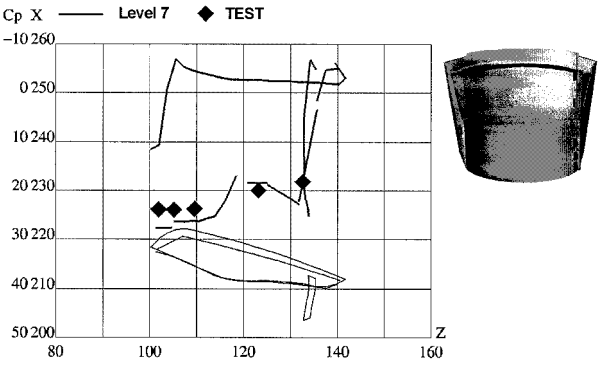

Fig. 5 Comparison of computed and experimental pressure distribution on reverser door for station 2 (Mach 0.15, ground effect).

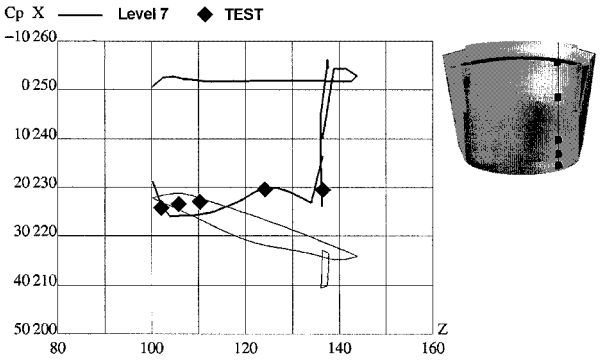

Fig. 6 Comparison of computed and experimental pressure distribution on reverser door for station 3 (Mach 0.15, ground effect).

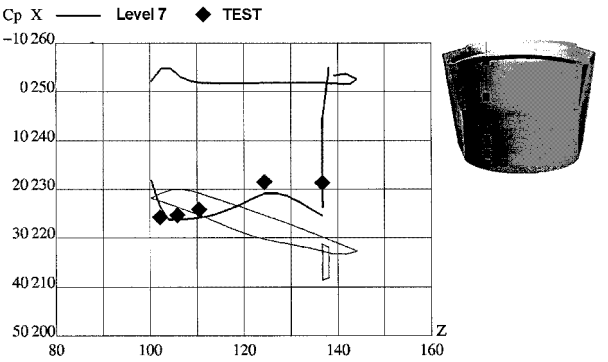

Fig. 7 Comparison of computed and experimental pressure distribution on reverser door for station 4 (Mach 0.15, ground effect).

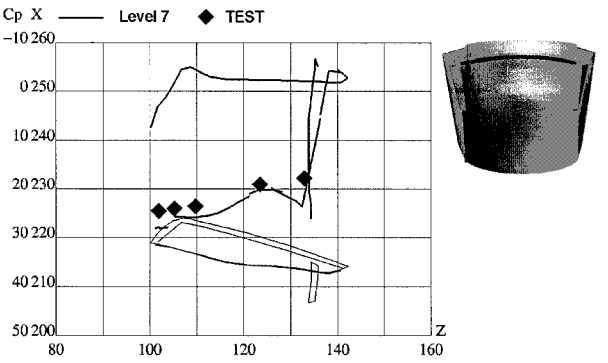

Fig. 8 Comparison of computed and experimental pressure distribution on reverser door for station 5 (Mach 0.15, ground effect).

indicated, further grid resolution improves the representation of a stagnation point at the base of the kicker plate and the associated adverse pressure gradient, but the Euler equations cannot predict the presence of the vortex that is due to viscous separation.

The lateral variation in geometry and surface pressure is shown in Figs. 5–8, which are ordered from inboard to outboard. The comparison to the test data degrades slightly toward the outboard side of the door. This degradation in the comparison is probably due to differences in flow leakage between the numerical simulation and experimental test. Specifically, the current numerical model does not include any door edge leakage in the region between the door and side beams. Furthermore, the fishtail door gap may not accurately reflect the gap detail included in the static model geometry or the numerical grid in this calculation may not correctly capture the fishtail leakage.

Door Loads

Because the thrust-reverser doors have sharp edges that provide fixed flow separation boundaries and produce a separated flow that is dominated by large-scale vortical structures, an Euler method is capable of accurately computing the total braking force. While viscous effects are undoubtedly important in determining the detailed pressure distribution on the lee side of the doors, the Euler method will capture the nominal pressure level on the aft faces for this case. Furthermore, because the door loads are predominately driven by the high-pressure jet, any errors in the aft face pressure distribution will not contribute significantly to the total braking force.

The total braking force has three primary elements, as summarized in Table 2. The present computations predict that 85% of the net braking force is associated with that part of the thrust-reverser doors facing into the engine exhaust plume. Here, the plume has traveled approximately one jet diameter downstream and is modeled adequately by inviscid equations. Integration of the aft-facing door pressures indicates that this component represents ~10% of the braking force. Consequently, these two components make up over 95% of the total braking force with the remaining contribution coming from the struts, core cowl, etc. The computed total single-engine integrated braking force acting on the engine components aft of the exhaust exit is 18,097 lb, which is about 2% higher than the test result.[7,8] Also, the measured reverser efficiency C_V is 35.9%, whereas the computed efficiency is 36.6%.

Convergence Studies

For a given grid cell size (or grid level), a measure of the degree to which the discretized flow equations are satisfied may be obtained by monitoring the order reduction in the L_2 norm of the solution residual. The standard procedure is to specify sufficient multigrid iterations (V-cycles) to achieve roughly an order of magnitude reduction in residual on each level.[10] The solution residual history for the Mach 0.15 case is presented in Fig. 9 for grid levels 4–7. Although some oscillatory behavior is apparent at each multigrid level, the final level 7 calculation attains nearly 1.6 orders reduction in residual. Furthermore, the solution history of total lift and drag coefficients at the finest level 7 grid solution exhibits less than 1% variation over the last 50 iterations (see Fig. 10).

Though critical to achieving a valid aerodynamic calculation, the previous discussion does not address the accuracy of the computed result. Flow quantities such as component or total lift and drag coefficients must also be monitored during the grid refinement process. A measure of the discretization error may be determined through this activity as the selected flow quantities approach asymptotic values with the addition of finer grid levels. In these simulations, the magnitude of the force exerted on the thrust-reverser doors as a result of the impinging exhaust plume is critical. The computed door braking force as a function of grid cell size is presented in Fig. 11. Here, the cell size relationship from a coarse-grid level to the next finer grid level is 1:2. Thus, level 3 represents one cell across the exit diameter, level 4 represents two cells, etc. It is noteworthy that the level 5 braking force is within about 3% of the level 7 calculation that contains cells that are four times finer. The computational time for the level 1–5 calculation is nearly one-tenth that of the time for the level 1–7 result. Consequently, preliminary predictions can be provided within 1–2 h of CPU time and final converged results on finer grid levels may be obtained by program restarts.

Simulation of key behavioral aspects of the exhaust plume, such as the centerline trajectory and plume expansion, are dependent on both accurate management of numerical dissipation and sufficient grid resolution. In reality, viscous effects at the boundary between the

Table 2 Component breakdown of computed total braking force[a]

Engine component	Braking force, lb	% of total
Thruster-reverser doors forward face	15,306	85
Thruster-reverser doors aft face	1860	10
Other components	931	5
Total	18,097	100

[a]Per engine.

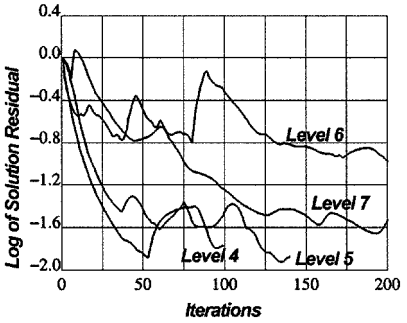

Fig. 9 History of solution residual for multigrid levels 4–7 (Mach 0.15, ground effect).

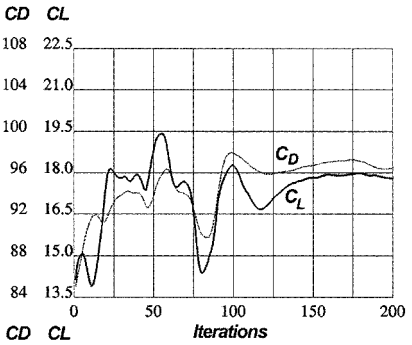

Fig. 10 History of lift and drag coefficient for the level 7 grid (Mach 0.15, ground effect).

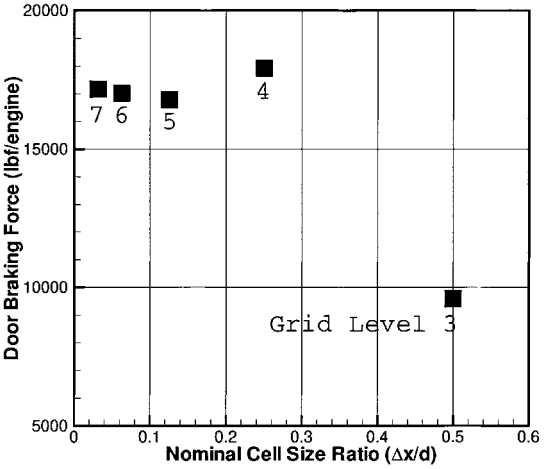

Fig. 11 Door braking force dependency on grid cell size.

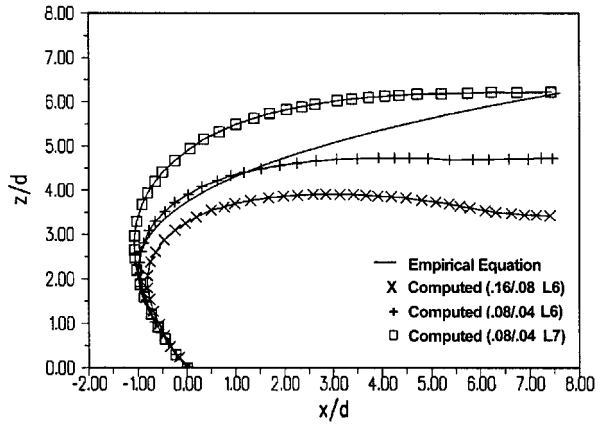

Fig. 12 Upper plume centerline trajectory dependency on grid resolution and dissipation levels (Mach 0.15, ground effect).

freestream and exhaust flows cause the plume to disappear at some location downstream. However, in the numerical method, artificial viscosity introduced to stabilize the Runge–Kutta iterations may lead to an unnaturally rapid decay of the exhaust plume. The current method utilizes a user-specified maximum and minimum level of the jump in normalized total enthalpy as a means of attenuating the dissipation level in the vicinity of the plume boundary.[10] A computed particle trajectory selected to best represent the plume centerline is compared in Fig. 12 with the analytical trajectory defined by Margason's equation.[11]

The trajectory displayed with the symbol "x" is computed with a max/min combination of 0.16 and 0.08 for the jump in total enthalpy, and represents higher overall numerical dissipation in comparison with the result with the symbol "+" (0.08/0.04 combination). In each case, the computations were conducted at grid level 6. The trajectory marked with the square symbol is at the reduced dissipation setting but at the finer level 7 grid resolution. These results indicate that although the coarser level 5 grid may be adequate for the estimation of the integrated braking force, accurate representation of the plume trajectory requires finer grid resolution. Because the plume wash in the vicinity of the horizontal tail was of interest in these calculations, the 0.08/0.04 total enthalpy combination with a level 7 grid resolution was selected. Finally, although the simulation of such crossflow plumes complicates the selection of the artificial viscosity magnitude, the reduced dissipation settings for these simulations still achieve stable, converged flow solutions.

Conclusions

A three-dimensional Cartesian grid Euler method is used to compute the flow about a contemporary business jet with thrust reversers deployed. While the entire aircraft is included in this simulation, the multigrid procedure facilitates grid refinement near the thrust-reverser components. Grid sensitivity studies and solution histories of residual, integrated force components, and surface pressures demonstrate that the Euler solution is stable and converged.

Calculations are completed for the aircraft with deployed thrust reversers in ground effect at a freestream Mach number of 0.15. Comparisons with wind-tunnel test data show that the computed exhaust plume geometry near the horizontal tail is qualitatively similar to that observed in tests on similar installations. Furthermore, the computed pressure distribution on the windward side of the upper thrust-reverser door compares favorably with the available test data. Quantitatively, the differences between the computed and measured pressures are about 10% for the lower three-quarters of the door and increase to roughly 30% at the base of the kicker plate.

Generally, these disagreements are most likely due to physical differences in the numerical and experimental models, and are related to flow leakage around the thrust-reverser doors. However, the Euler method also fails to predict the presence of a vortex at the base of the kicker plate, which is due to viscous effects and is observed in the experiment. Still, the computed net braking force is within 2% of the measured data for the Mach 0.15 ground effect condition, and the Euler calculation indicates that ~85% of the braking force is generated on the windward side of the thrust-reverser doors.

These calculations include approximately 2×10^6 grid points, with most of the grid concentrated near the nacelles. Fortunately, the simple Cartesian grid structure facilitates an initial problem preparation time of only a few days and a complete aerodynamic solution for this ground effect simulation may be achieved in approximately 18 h on a Cray J90. On the other hand, only slightly less accurate, preliminary thrust-reverser loads can be obtained with this method in 1–2 h of compute time and final converged loads achieved by program restarts. Furthermore, minimal effort is required to obtain solutions at other engine flow settings or onset flow conditions and only minor grid adjustments are necessary to analyze an additional door angle or kicker-plate geometry. These key features support the application of this Euler method for installed thrust-reverser analysis at the preliminary design stage.

Acknowledgments

The authors would like to recognize the contributions of their colleagues at Analytical Methods, Inc., and Israel Aircraft Industries toward the success of this work. Further, the authors would like to thank Jef Dawson and David Whitaker of Cray Research for providing valuable computer time and for their work in vectorizing the code.

References

[1] Van Hengst, J., "Aerodynamic Integration of Thrust Reverser on the Fokker 100," *Proceedings of the Conference on Propulsion/Airframe Integration*, CP 498, AGARD, 1992, pp 10.1–10.9.

[2] Imlay, S. T., "Numerical Solution of 2-D Thrust Reversing and Thrust Vectoring Nozzle Flowfields," AIAA Paper 86-0203, Jan. 1986.

[3] "Static Performance of Several Novel Thrust Reverser Concepts for Subsonic Transport Applications," AIAA Paper 96-2649, July 1996.

[4] Lecordix, J. L., Gippet, J. M., and Duparcq, H. L., "Design of an Advanced Nacelle for a Very High Bypass Ratio Engine," *Aeronautical Journal*, Vol. 96, Dec. 1992, p. 387.

[5] Hebert, L. J., and Ponsonby, R. E., "Applications of CFD Technology to the Design of Aircraft Propulsion Systems," *AIAA/ICAS-90-5.4.1*, Sept. 1990.

[6] Epstein, B., Luntz, A., and Nachshon, A., "Multigrid Euler Solver About Aircraft Configurations, with Cartesian Grids and Local Refinement," AIAA Paper 89-1960, June 1989.

[7] Van Nunen, J. W. G., Kooi, J. W., and Takens, J., "Wind Tunnel Investigations of the Effect of Thrust Reversers on the Stability and Control Characteristics," Duits-Nederlandse Windtunnel, Rept. DNW-TR-94.04, May 1994.

[8] Hutton, P., "BR710-48/1:12 Scale Installed Thrust Reverser Model Tests at DNW, Holland," BMW/Rolls-Royce, Rept. 1AR51029, Issue 1, May 1995.

[9] Frank, J. H., Meyer, P., and Henger, C., "BR710 Thrust Reverser Static Isolated Scale Model Aerodynamic Compliance Tests (SISMAC) at FluiDyne, Minneapolis, Test Report," Hurel-Dubois Document 94-42570A, Oct. 1994.

[10] Margason, R. J., "The Path of a Jet Directed at Large Angles to a Subsonic Free Stream," NASA TN D-4919, Nov. 1968.

[11] *MGAERO User's Manual, Version 3.0*, Analytical Methods, Inc., Redmond, WA, 1996.